Title: "Experimental Investigation of Force Balance at Vapour Condensation on a Cylindrical Fin"

Andrey Glushchuk[1,*], Christophe Minetti[1], Hatim Machrafi[1,2], Carlo S. Iorio[1]

[1]Microgravity Research Centre, Université libre de Bruxelles, Avenue F. Roosevelt 50, 1050, Bruxelles, Belgium
[2]University of Liege, Thermodynamics of Irreversible Phenomena, Allée du 6-Août 19, 4000, Liege, Belgium

* Corresponding author
E-mails: aglushch@ulb.ac.be (A. Glushchuk), cminetti@ulb.ac.be (Ch. Minetti), h.machrafi@ulg.ac.be (H. Machrafi), ciorio@ulb.ac.be (C. S. Iorio)

Abstract:

Experimental investigation of vapour condensation on single cylindrical fin has been carried out under various gravity conditions: $1g_0$, $1.8g_0$ and $0.05g_0$. For the first time, a balance of forces acting on the condensate flow is analyzed. The fin surface is divided in seven areas, each one being characterized by the main force acting on the liquid motion: gravitational vs surface-tension pressure gradient. The magnitude of the areas does not depend on the gravity level. This confirms the correctness of the fin surface segmentation, as used by various authors, to simplify the condensation modelling. It has been shown that the most intensive vapour condensation takes place in the areas, where the surface-tension pressure gradient is higher than the gravity force. Analysis of the heat load shows that each region affected by STPG provides 10-15 % of the total heat load, a contribution that is not negligible and should be taken into account. In case of low gravity, the most intensive condensation takes place at the corner of the fin tip, where the curvature gradient is maximum, and on its cylindrical part. The heat loads in these regions are comparable.

Key worlds: condensation; gravity; force balance; cylindrical fin; surface-tension; curvature gradient

Nomenclature

Symbols

Cp	specific heat
f	focal length
g	gravitational acceleration
g_0	normal gravitational acceleration, 9.8 m^2/s
G	mass flow
J	net mass flux
l	length
M	molar mass
P, p	pressure
q	heat flux
Q	heat removed per unit time
R	thermal resistance
R_0	universal gas constant, 8.3144598 J/(mol K)
s, S	arc length
T	temperature
T_{cp}	temperature of cold plate
T_{Ph}	temperature of fin-sample base
T_{tc}	air temperature
U	overall heat transfer coefficient
X	abscissa
Y	ordinate

Greek symbols

α	heat transfer coefficient
δ	thickness
Δ	difference
φ	angle of tangent direction
κ	curvature
λ	thermal conductivity
θ	turn angle of surface arc
ρ	density
σ	surface tension

Subscripts

as	axial symmetry
c	capillary
$cond$	condensation side
f	fin
fs	fin surface
hp	heat pipe
l	liquid
tot	total
sat	saturation
v	vapour
w	water

1. Introduction

The enhanced heat transfer tubes for vapour condensation is widely used, e.g. in refrigeration, air conditioning, petroleum and food industry etc. A widely used intensification method is the finning of the tube surface. The enhancement is provided not only by increasing the contact area between the vapour and the colder surface but also by the action of surface tension forces, which help to move a condensate from the fin additionally to other forces (gravitational, shear stress, …). If a liquid–vapour interface is curved, a pressure difference across the interface must be present to establish a mechanical balance. The balance is described by the curvature (κ_{tot}) of the liquid-vapour interface within the Young-Laplace equation:

$$P_l-P_v=\sigma\kappa_{tot} \quad (1)$$

Any curvature variation along the interface induces a pressure inhomogeneity within the liquid which leads to fluid redistribution. This pressure variation is known as the surface-tension pressure gradient (STPG). The fin shape influences the condensate film flowing along the fin surface. This leads to the arising of STPG, which effects on the film flow. The expression for the STPG can be obtained by differentiating the equation (1) with respect to the film surface arc length (s):

$$dP/ds=\sigma\cdot d\kappa_{tot}/ds \quad (2)$$

It means that STPG is presented in the condensate flowing along any fin, because each fin shape has corners and/or roundings. This fact reveals two main problems in the theoretical description of vapour condensation on the finned surface. First of all, the fin shape becomes one of the parameters in the modelling that complicates the simulation, considering the big variety of possible profiles. Secondly, there are some difficulties with the validation of existing models.

Many efforts can be found in the literature focusing on the investigation of condensation on the outside of horizontal finned tubes. Comprehensive overview can be found in the book of Rifert and Smirnov [1] and some review papers [2 – 3]. Three classes of prediction models exist based on various approaches: semi-empirical, numerical and surface segmentation. Semi-empirical models are based on the already obtained experimental data and on a conception of the condensate film behavior [4, 5]. They provide a very good prediction only for fluids and fin shapes contained in the data base used. Numerical models using Navier-Stokes equations together with the heat balance equation [6, 7], not only predict the heat transfer but also the behavior of condensate film on the finned surface. Unfortunately, they require a very detailed description of the fin profile and time consumption of the calculation is very high. A third class of models is based on the subdividing of the condensation surface into areas with different approaches of the heat transfer [8 - 10]. This way of modeling is very adaptive to any fin shape. However, the results are very sensitive to the segmentation algorithm. Such variety of different modeling ways and various calculation algorithms are the result of the lack of any reliable information about condensate flow on the fin. Furthermore, almost all models provide the same level of prediction uncertainty of the average heat transfer coefficient within 15 - 20%, which complicates their verification.

Mainly, experiments are carried out on long tubes (several meters) in order to make an "averaging" on fins and minimize the effect of fin imperfections on the condensation. Indeed, the same fin shape cannot be reproduced along the tube because of non-perfections of the manufacturing processes, of worn cutting tools used, etc. Therefore, a large number of fins is used in the experiments. Generally, the tube is cooled by water flowing inside. Temperatures of water at both inlet and outlet are measured. Heat removed from the tube per unit time Q is measured by the standard calorimetric method:

$$Q= Cp_w\cdot G_w\cdot\Delta T_w \quad (3)$$

3

Here Cp_w is water specific heat, G_w is mass flow of water and ΔT_w is temperature difference at both tube ends. Temperature and pressure of the vapour are maintained stable. An averaged heat transfer coefficient is evaluated using the Wilson plot method based on analysis of overall thermal resistance of the global heat transmission process [11 - 13]. The overall heat transfer resistance can be written in steady state as:

$$1/U = 1/\alpha_{cond} + R_{tube} + 1/\alpha_w \qquad (4)$$

Here, U is the overall heat transfer coefficient, α_{cond} is heat transfer coefficient (HTC) on vapour side, R_{tube} is the tube thermal resistance, and α_w is HTC of the water flow. R_{tube} is inversely proportional to the tube thermal conductivity and, therefore, is constant (neglecting any temperature dependencies). Typically, α_{water} is varied by manipulating with the water flow and the overall HTC is measured in the experiments. Although equations (3) and (4) are rather standard, they still allow emphasizing the inconsistency of literature data obtained with this method and are also used for the verification of the existing condensation models. Figure 1 demonstrates the condensation experiment with the tube having rectangular finning. Condensation HTC is evaluated from equation (4). Detailed description of the experimental procedures and data reduction algorithms can be found in the present papers of Fernandez-Seara et al. [14] and Ji et al. [15]. Such type of experiments provides an accuracy of about 15-25 % of the average heat transfer coefficient measurement. This makes the obtained data to be very useful in engineering. However, the provided accuracy is not enough to validate models which have similar uncertainty of prediction.
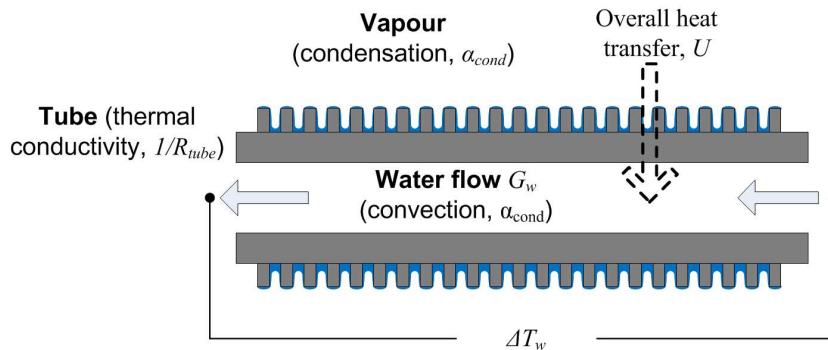

Figure 1. Schematic of the condensation experiment with the tube having rectangular finning.

The local data about the condensate behavior on the fin and the liquid flow between fins are very important for improvement of existing models and validation of the approaches made. Some scientific teams tried to use the original concepts of experiments to obtain any information about condensation on the fins [16, 17]. S. Hirasawa with colleagues [16] has performed experimental simulations on collecting condensate between two rectangular fins. In their geometry, the liquid film was flowing along a vertical open channel. The channel width was decreasing from top to bottom. There, the flow dynamics of the liquid flow from the fin to the space between the fins has been observed and described. The local thinning in the area between the thin film and the meniscus has been observed. It has been shown in [16] that the thinning of the liquid film on the fins produces a local acceleration of the transverse flow. But their experiment does not take into account the flow of condensed vapor through the free surface of the film which can thicken the liquid film.

M. A. Kedzierski and R. L. Webb [17] have investigated condensation on vertical plates having various longitudinal finning. Fins with constant radii (0.4 and 0.8 mm), with curvilinear tips, of different heights and with special design ("Gewa-T") were tested. Fins were accurately machined on vertical plates with accuracy ±3 µm using the electric discharge process. Plates were made of cupper. Authors found that fins without any changes of surface curvature provides poorest average heat transfer coefficient. Fins with curved tip showed the same condensation capability as Gewa-T. Improved Wilson plot technique was used to extract the heat loads at the fin tip and the

lateral part from the total heat measured for the curvilinear fins. Heat transfer data proved that the curvature gradient dictates the drainage force of the film on the tip. It was found that the dependence of HTC on the lateral part from the temperature load diverges from the Nusselt theory. The authors [17] conjectured that gravity was not the main driving force in this region. Unfortunately, they gave only qualitative analysis of the forces acting on the condensate film in the dedicated case of fins with curvilinear tip.

Recently, Glushchuk et al. [18] proposed a new way of experimental investigation of the condensate flow along the curved fin. The capillary constant of the liquid l_c describes the scale of any system where surface tension force has the same order of magnitude as gravitational one:

$$l_c = (\sigma/\rho g)^{0.5} \quad (5)$$

Here σ is surface tension, ρ is liquid density and g is gravitational acceleration. Usually, the capillary constant is several millimetres for the majority of fluids of interest in condensers. Therefore, the typical height of fins used in condensers is less than 2 mm. The authors [18] proposed to carry out the experiments under reduced gravity conditions to have larger capillary constants and, as a result, to observe the effect of surface-tension force on bigger fins. An axisymmetric curvilinear fin with height 16 mm was used. A dedicated optical system has been developed to measure the condensate film on the fin with an accuracy of around 6 μm. It has been found that the film thickness increases with reduced gravity level. Local thinning of the film in the area between thin film and meniscus was observed. Unfortunately, the steady state condition of vapour condensation was not reached during the low gravity period.

In the present work, experimental investigation of condensation of pure vapour on single cylindrical fin has been carried out under various gravity conditions. The goal is the evaluation of a balance between gravitational force and the surface tension pressure gradient (STPG) along the fin surface and revealing of areas where one of these forces affects strongly on the condensate motion. The second task is to reveal a correlation between heat transfer differences in the various areas on the fin and the acting force.
Such king of information does not exist in the literature and allows to examine the existing ways of the modelling.

2. Concept of the parabolic flight experiment

A parabolic flight is a ballistic trajectory by a modified aircraft during which a short period of around 22 seconds of low gravity at $0.05g_0$ is experienced. Just before and after the low gravity period two periods of around 20 seconds each of hyper gravity at around 1.5-$1.8g_0$ are also experienced. ESA parabolic flights are carried out with an Airbus A300 aircraft known also as Zero-G, which flies out of the Bordeaux-Mérignac airport in France. Detailed description of the gravity conditions during one parabolic manoeuvre is presented in the paper of V. Pletser [19]. The ESA campaign is run over three days and on each day thirty parabolas are performed.

The key point of any experiment during parabolic flight is reaching a steady state condition or, at least, a stable behaviour. Therefore special attention should be taken for the conceptual formulation of an experimental study. The idea of the presented investigation is that the condensate flows down from the cell by gravity at hyper and normal gravity and accumulates on a cover during 22 seconds of low gravity period (Figure 2). The cover closes fin cooling system. Elimination of an active system that retracts the condensed liquid simplifies considerably the set-up and, as a result, decreases the time required for the process stabilization.
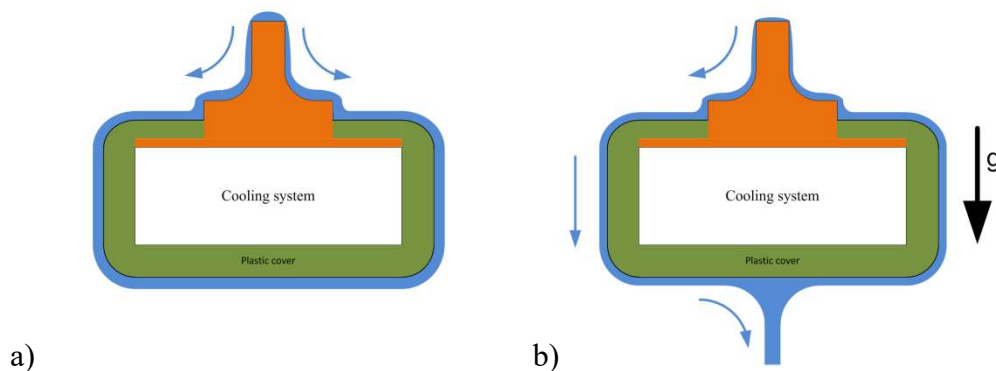

Figure 2. Condensate flow under low gravity condition (a) and at hyper and normal gravity (b).

3. Description of the set-up

3.1 Experimental apparatus

The experimental set-up is schematically shown in Figure 3. The set-up consists of a condensation-evaporation container (1), an external thermo-stabilization container (2), a heat dissipation system (3), a magnetic stirring machine (4), an afocal optical system (5), a camera with a light source (6), a test cell (7)and a data acquisition system (PC1 and PC2).

The design of the main container (1) is based on the thermosiphon principle. Evaporation and condensation happen in the same sealed volume. The container has two chambers separated by a partition with a central opening. Such a concept reduces the number of connections between an evaporator and a condenser. This minimizes the penetration of non-condensable gases from air into the experimental volume. A condensation test cell is installed in the upper chamber, while the evaporator is located in the lower one. The evaporator is filled with a refrigerant. During the experiment, the partition allows for the recuperation of the vapour condensed during the experiment. The side wall of the evaporator is made out of a transparent tube with an inner diameter of 104 mm and a height of 30 mm. The bottom wall of the evaporator is made out of aluminium. The condenser part of the experimental cell is a rectangular box with dimensions of $145\times145\times90$ mm^3 (L×W×H). The front, back and bottom walls are made of strong opaque plastic (PEEK) providing rigidness of the construction. Other walls are transparent and made of polycarbonate (LEXAN). Two optically transparent windows are installed at the lateral walls of the condensation chamber (Figure 3). A double glass configuration for the windows is used in order to avoid the

appearance of the condensate film on them because of natural convection. Silicon sealant is used to seal all parts of the container.

The wall separating the evaporator and the condenser has a circular orifice at the centre, in which a fluid barrier is inserted. The barrier for the liquid is made out of aluminium in the form of a hollow cylinder with a sharp edge at the bottom and the flange at the top.

Heat to vaporise the working fluid is generated by the heating magnetic stirring machine located under the container (see Figure 3). The rotary motion is transmitted to the fluid with a magnetic stirrer contained inside the evaporator chamber. The liquid inside the evaporator chamber is kept in rotation to prevent, during microgravity, that the same liquid spills inside the upper chamber where the condenser is located. The camera is used for visualization of the liquid behaviour in the evaporator and for detection of the liquid entering the condensation volume. Detailed description of the evaporator functionality is presented in the paper of Buffone et al [20].

The inner experimental container is mounted into the thermo-stabilization container (2). Three nichrome-wired electrical heaters and eight fans warm the air in between the two containers up to the operating temperature of the vapour minimizing the heat losses and getting rid of unwanted condensation on the internal walls of the main container. The external container is leak-tight.

The heat released during condensation is removed from the container and dissipated to ambient air by means of two screen mesh heat pipes and a fan-cooled thermoelectric assembly (TEA), as schematically shown on the left-hand-side of Figure 3. A PID controller is used to provide a stable temperature of the heat pipes part inserted into the test cell.

Vapour temperatures at two levels inside the condensation chamber (T_{v1} and T_{v2}) were measured by platinum resistance thermometers (PT-100), individually calibrated to reach an accuracy of ±0.02 K. The vapour pressure (P_v) was measured with an accuracy of 0.6 hPa. Thermistors (5kΩ) were used for monitoring the walls' temperature of the internal container (T_{left}, T_{right}, …), the temperature of the evaporator bottom (T_h) and the average temperature of the air inside the thermo-stabilization container (T_{tc}), all within an accuracy of ±0.5 K.
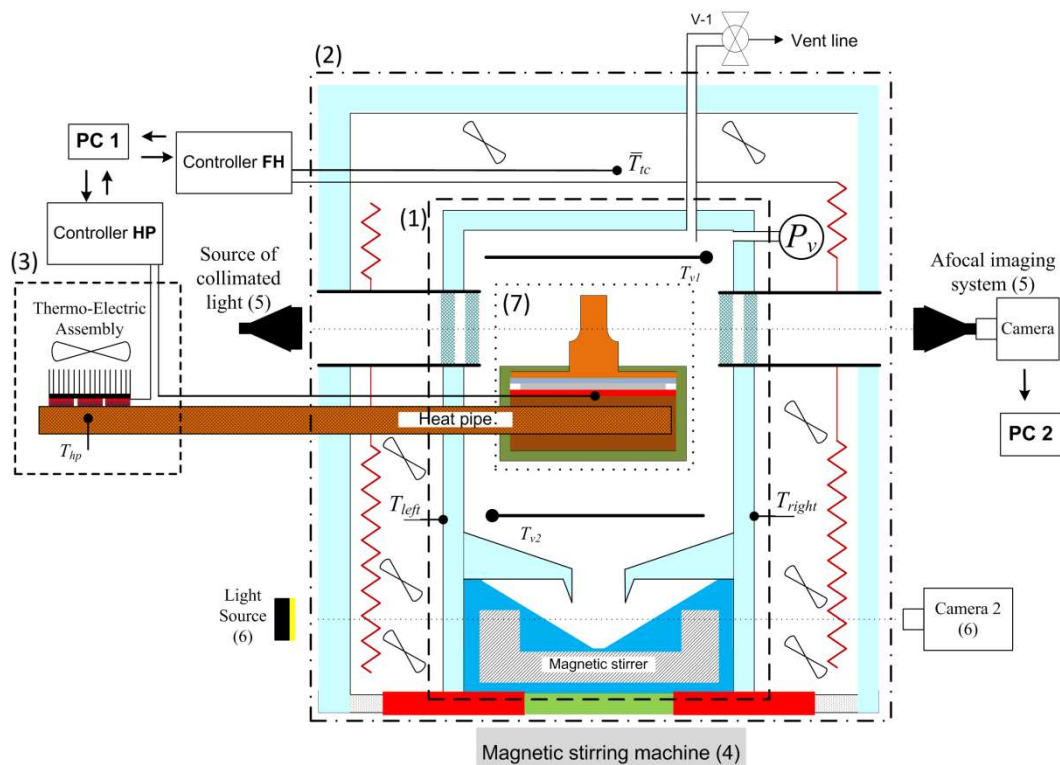

Figure 3. Schematic of experimental set-up.
(1) condensation-evaporation container; (2) external thermo-stabilization container;
(3) heat dissipation system; (4) a magnetic stirring machine; (5) afocal optical system; (6) camera with light source;
(7) test cell; (PC1 and PC2) data acquisition system.

The test cell is composed of a fin-sample, a thermo-electrical module (TEM), a cold plate and a cover. Figure 4 shows a drawing of the cell. The fin-sample is a metallic part composed of three segments: a condensation surface further called simply "fin", a pedestal and a base. The fin-sample together with the TEM is mounted on the cold plate. The heat pipes are inserted into this plate. The cover (green box in Figure 4) closes almost all components of the test cell except the condensation surface and is made of a low conductive plastic (TEFLON). Therefore it is assumed that condensation happens only on the fin surface.

The TEM is used to maintain the temperature of the fin-sample base (T_{Ph}) at the selected level. The temperature is adjusted by PID controlling by PC1 the electrical current passing through the thermo-electrical module. Decoupling the fin-sample from the massive heat dissipation system by introducing the TEM dramatically reduces the time response of the test cell and provides a stable condition within the 22 seconds of the low gravity period. Stabilization of the process is discussed in details in section V.

The temperature distribution inside the fin-sample body was measured by four 10kΩ thermistors. The thermistors have an accuracy of 0.1 K. The sensors were located in holes drilled into the fin-sample (see Figure 4), providing contact with the metallic body by a low conductive insert made of TEFLON.
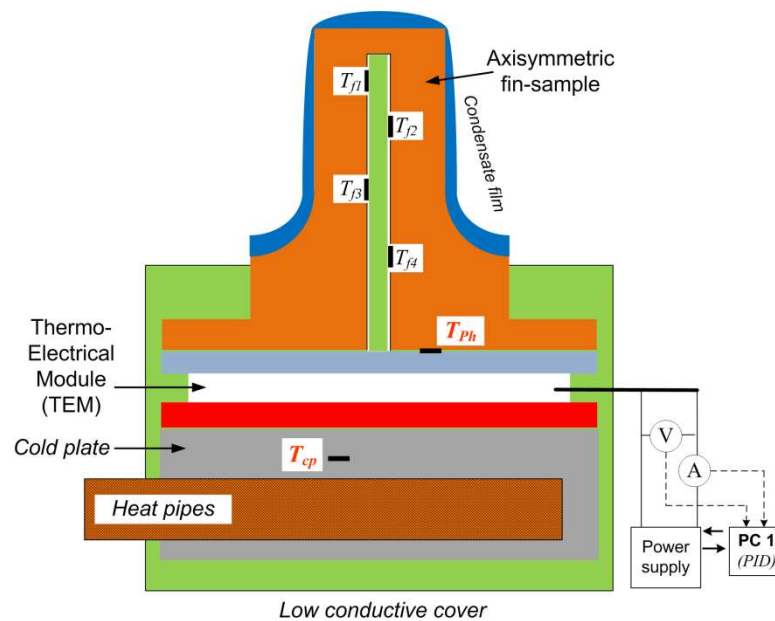

Figure 4. Drawing of test cell.

3.2 Afocal system for film thickness measurement

The optical afocal system for film thickness measurement has been developed and is reported schematically in Figure 5. It is composed (from left to right) of a light source, an aperture, a collimating lens, the object under investigation, a focusing lens, a light filter, an objective lens, and a CCD camera. As depicted in Figure 5, the optical system images the fin profile on the CCD camera. The light emerging from a red Led (630 nm) is filtered by an aperture and collimated by a lens (f=300 mm) to illuminate the fin with a plane wave. The fin is then imaged on the sensor of the camera by an afocal system made of two lenses (with focal lengths of respectively 150 and 50 mm). The spatial resolution of the system is 6.3 µm/pixel and the resolution of the camera sensor is 2592×1944 pixels^2. Enhanced accuracy is obtained by slightly defocusing the imaging system in such a way that a diffraction pattern appears around the fin. This diffraction pattern is then used to enhance the resolution and get sub-pixel accuracy [18]. The film thickness is obtained by comparing each point of the imaged fin contour with and without the liquid. Detailed description of the system can be found in [18].
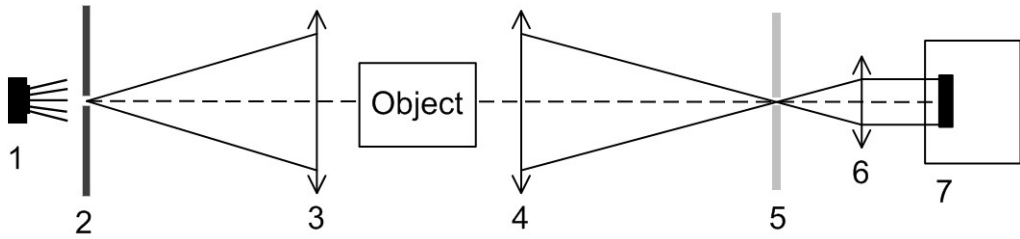
Figure 5. Schematic diagram of the afocal system.
1) light source; 2) aperture; 3) collimating lens;
4) focusing lens; 5) light filter; 6) objective lens; 7) CCD camera.

3.3 *Cylindrical fin*

Error! Reference source not found. shows a photo (a) and a cross section profile (b) of the brass fin-sample used during this campaign. The profile was measured by the afocal system. The condensation surface (fin) consists of an axisymmetric cylindrical part and a curvilinear bottom (**Error! Reference source not found.**b). The fin was polished to reach a mirror-like surface with roughness level lower than 1 μm. The height of the fin is 8.9 mm and the diameter of its cylindrical part is 5.9 mm (curvature 339 m^{-1}). A corner at the fin tip is rounded. The radius of the curvilinear part is 3 mm (curvature 333 m^{-1}). The height and the diameter of the pedestal are 9 mm and 17.9 mm, respectively. The diameter of the hole inside is 2.4 mm. Black circles on the **Error! Reference source not found.**(b) visualise the locations of the temperature sensors. The thermistors are positioned at 20 mm (T_{f1}), 18 mm (T_{f2}) and 11.5 mm (T_{f4}) from the fin-sample base.
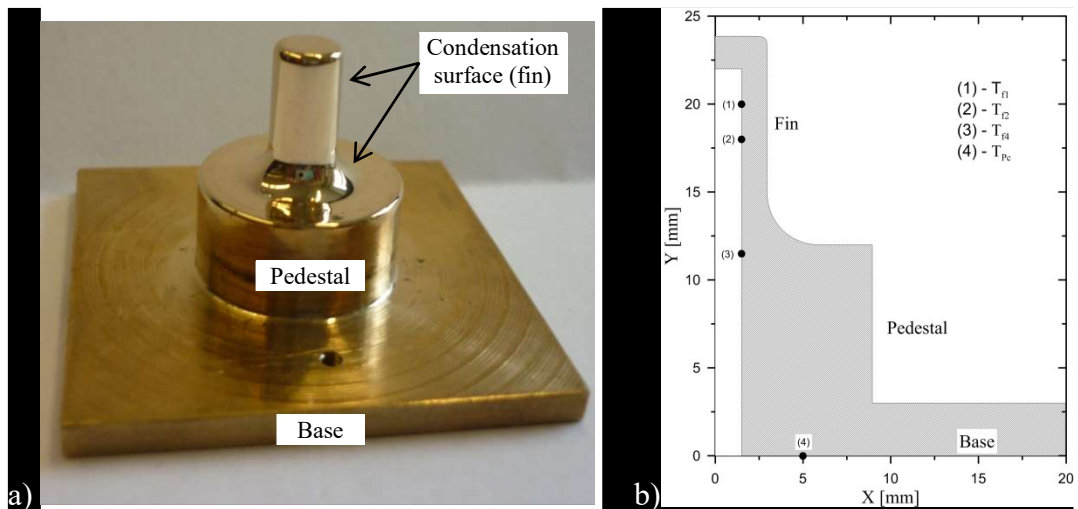

Figure 6. Photo (a) and cross-section (b) of fin-sample;
Black circles show location of the temperature sensors.

3.4 *Experimental procedures*

A special purification procedure has been carried out to remove all non-condensable gases from the internal container. The experimental procedure can be summarised as follows:

1. First of all, the evaporator is filled completely with the liquid (HFE-7100) through the front cover.
2. After sealing the container, the air-vapour mixture is pumped out from the condensation chamber until the liquid starts boiling.
3. The heating of the evaporator and the cooling of the fin-sample are initiated. The purification method is based on the boiling and subsequent condensation of the vapour in the closed volume. Non-condensable gasses contained in the liquid are released and accumulate in the upper part of the cell.
4. The gas-vapour mixture is pumped out periodically every 30 minutes. Generally, 4-6 cycles of pumping out are enough to obtain the vapour with gas mole fraction less than

1%, and a corresponding mass concentration of 0.09%. These values are obtained by measuring the pressure and temperature at the same location and comparing it with the saturation pressure. The difference between the measured saturation temperature and the temperature obtained by measuring the pressure after degassing, has been found to be around 0.03 K.

5. Finally, at this stage, the condensation experiments can be performed.

4. Curvature and surface temperature calculations

4.1 Curvature calculation

The condensate film moves under action of two forces: gravity and gradient of capillary pressure inside the film. Gravity level is known from the acceleration measurements in the plane. The distribution of the film surface curvature should be evaluated in order to estimate the second force. Total curvature of the surface consists of two terms: $\kappa_{tot}=\kappa_{fs}+\kappa_{as}$. The first term κ_{fs} corresponds to the change of the surface profile and is calculated using the following formula:

$$\kappa_{fs} = \Delta\varphi/S \qquad (6)$$

where $\Delta\varphi$ is an angle of tangent direction change at the segment which has length S (**Error! Reference source not found.**). Second part of the total curvature κ_{as} is a result of axial symmetry of the film on the fin and is calculated as:

$$\kappa_{as}= \sin(\theta)/(X-X_0) \qquad (7)$$

Here, θ is the turn angle of the surface arc, X is the abscissa of the surface and X_0 the symmetry center position (**Error! Reference source not found.**).

The algorithm for the total curvature calculation consists of 10 steps:

1) The center of symmetry of the film profile measured by the optical system is identified;
2) Each side (left, right) of the profile is segmented into N sections;
3) Vector of tangent direction is calculated at each knot between the sections;
4) Angle between the tangent vectors is estimated at each section;
5) Length of each segments is determined;
6) First term of the curvature is calculated for each segment;
7) X coordinate of the segment center is obtained;
8) Calculation of the turn angle;
9) Second term of the curvature is calculated;
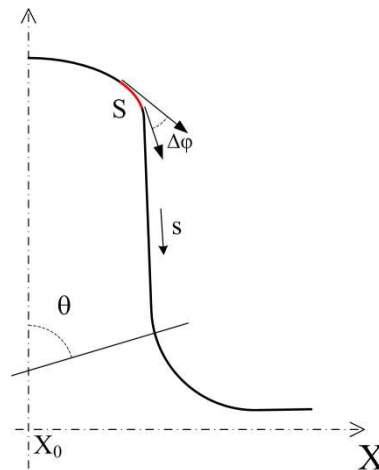10) Calculation of the total curvature.

Figure 7. Parameters used in curvature calculation.

Error! Reference source not found.a shows the fin surface curvature calculated using the algorithm described abouve. Vertical dashed line marks the center of the fin corner. The arc length is measured from the axis symmetry of the fin. **Error! Reference source not found.**b visualizes the arc length values on the fin surface. The center of the fin corner is located at the arc length 2.9 mm. Black rhombs in **Error! Reference source not found.**a correspond to the curvature of the fin profile κ_{fs}. Grey circles show the second curvature κ_{as} of the fin surface. The black line is the total curvature. The curvature of the fin tip is equal to zero (**Error! Reference source not found.**, arc length 0 - 2 mm) and the lateral wall has a cylindrical shape with a curvature of 338 m^{-1} (**Error! Reference source not found.**, arc length 4 - 11 mm), as expected. Profile analysis reveals that the fin corner does not have a perfect semicircular shape. The total curvature changes from the maximum value (about 2450 m^{-1}) at the corner to zero at a length of about 1.2 mm for the left side and a length of 1.1 mm on the right side (**Error! Reference source not found.**a, rhombs). Transition from the lateral wall to the curved fin bottom occurs between 11 mm and 12 mm of the surface arc length. It is interesting to mention that the profile curvature of the curved part of the fin has a non-varying value of 338 m^{-1} (**Error! Reference source not found.**a, arc length 12-15 mm), whereas the total curvature decreases slowly.
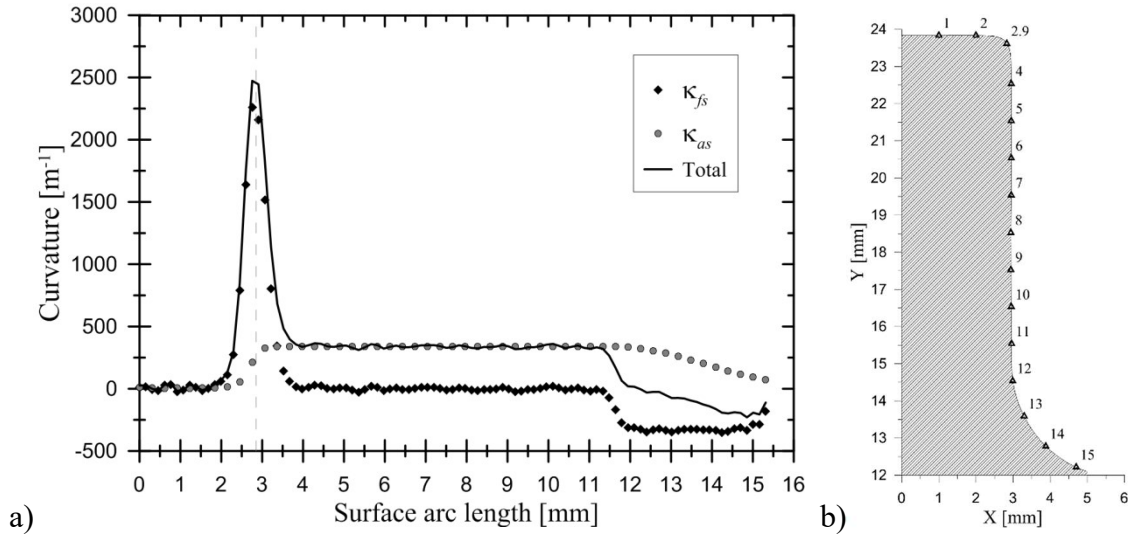
Figure 8. Curvature of the fin surface (a) and visualization of the arc length (triangles) of the fin surface (b); Dashed line shows location of the fin corner center.

4.2 Temperature calculation

For the temperature calculations of the fin surface, we used a CFD code, implementing a geometry corresponding to the exact shape of the fin and the liquid film (obtained from optic measurements) as depicted by the orange and blue parts of Fig. 3. The mesh of the geometry is sufficiently fine so that a higher mesh density only results into a difference of the calculated temperatures of less than 0.1 K (corresponding to the measuring uncertainty of the thermistors). We used a finite element method for the calculations using the Comsol software with a 2D axisymmetric model. The model included heat transfer in both solids and liquids. The boundary conditions of all the temperatures are dictated by the experimental conditions. The condensation at the liquid-vapour interface is simulated by assuming that we are dealing with a vapour that behaves as an ideal gas. Furthermore, the vapour phase is assumed to be sufficiently close to equilibrium. The liquid-vapour interface is assumed to behave as a Knudsen layer, entrapped in between the liquid and the vapour phases [21]. The condensation is then mathematically simulated as the net value from the evaporation rate and the condensation rate, respectively from the liquid phase to the gas one and vice versa. From kinetic considerations (assuming the possibility of using Boltzmann's equation of kinetic theory), we end up, in line with [22], with the following expression

$$J = \sqrt{\frac{M}{2\pi R}} \left[\frac{p_{sat}(T_l)}{\sqrt{T_l + 273.15}} - \frac{p(T_v)}{\sqrt{T_v + 273.15}} \right] \quad (8)$$

11

where J is the net mass flux (in the conditions of this work, the net condensation rate), M the molar mass, R_0 the universal gas constant, $p_{sat}(T_l)$ the saturation pressure at the liquid-side temperature (T_l) of the interface and $p(T_v)$ the vapour pressure at the gas-side temperature (T_v) of the interface. By means of an energy balance at the interface (taking into account heat conduction through the gas phase, albeit negligible), gives the heat transfer to the liquid. Adding heat conduction through the liquid and heat conduction through the fin for mathematical closure gives finally the temperature at the fin surface. In order to verify the validity of the model, we compared the computed temperatures at the inside of the fin (corresponding to the temperature sensors in Figure 6) to the ones measured experimentally. The maximum difference between the simulated and experimentally measured temperatures is 0.4 K. Knowing that the thermistor accuracy is 0.1 - 0.2 K, the CFD model is considered satisfactorily validated and will be used to back up some experimental interpretations.

5. Experimental results and discussion

The investigation of vapour condensation on a cylindrical fin under various gravity conditions has been carried out during the 61st ESA parabolic flight campaign.

HFE-7100 has been used in all experiments because of its relatively low latent heat value (111 kJ/kg), and low boiling point (61 °C), with respect to water. HFE-7100 is the commercial name of 3M's engineered fluid methoxy-nonafluorobutane (C4F9OCH3). It is a clear, colourless and low-odour fluid intended to replace ozone-depleting substances (ODSs) and compounds with high global warming potential (GWP) in many applications. The properties of the liquid used are reported in table 2. All information about the properties provided can be found in [23].

Properties	Value
Chemical formula	$C_4F_9OCH_3$
Molecular Weight, g/mol	250
Boiling Point (1 atm.), °C	61
Heat of Vaporization (20 °C), kJ/kg	124
Liquid density (20 °C), kg/m^3	1493
Surface Tension (20 °C), N/m	0.015
Liquid thermal conductivity (20 °C), W/(mK)	0.07
liquid specific heat (20 °C), J/(kgK)	1173

Table 2. Physical properties of working fluids (HFE 7100).

The temperature of the vapour was maintained in the range of 45 – 55 °C. Corresponding vapour pressures are within 600 – 800 hPa. This was only a little less than the pressure in the airplane cabin (~800 hPa), which minimized the possibility of air penetration into the condensation chamber. The temperature of the inner test cell walls was maintained at 60 °C to prevent heat losses to the ambient atmosphere and condensation on the optical windows. The temperature of the cold plate was maintained stable during all experiments. The temperature of the fin-sample base was changed each two or three parabolas.

Figure 9 shows profiles of the condensate on the fin captured by the optical system during one parabola. The area occupied by the liquid is indicated by a blue color in the figure. The vapour pressure was 635 hPa. The temperature evolution measured inside the fin-sample is shown in Figure 10. In normal gravity, the condensed fluid flowed down back to the evaporator. A slightly squeezed drop was detected on the fin tip (Figure 9a). A thin film was observed along the lateral wall and stable temperature distribution was reached (Figure 10, -40 ... -26 s). During the first hyper-gravity period, the film became thinner (Figure 9b). The drop at the tip was flattened and the liquid level at the fin bottom was lower than at normal gravity. A slow growth of the fin

temperature was observed (Figure 10, hyper gravity). It means that more heat was transmitted through the fin. Under low-gravity conditions, the condensed liquid was accumulating on the test cell surface, as was designed. The drop had an ideal shape of a hemi-sphere and it grew nonlinearly during the whole period. Growth of the liquid level at the fin bottom was observed. The film was thick on the lateral wall of the fin (Figure 9c). The temperature decreased at the beginning of the low-gravity period (Figure 10, 0…5 s), but it stabilized at the end. It means that growth of the liquid amount on the tip and at the bottom of the fin did not affect the condensation heat transfer. These areas played a role of the condensate accumulators only. A strange behavior of the fin-sample body temperatures during low gravity period (Figure 10) is resulted by PID maintenance of its base temperature. Optical observation showed that the condensate film was very sensitive to any external disturbance, such as: airplane vibration, movement of people in the cabin, neighboring experiments.

Condensation is a slow process, contrary to boiling. It is difficult to reach a steady state condition within 22 seconds. Only "stable" condition was achieved in the presented investigation, by which we mean that no significant increase or decrease of the measured quantities occurs. This concerns three criteria being used to describe such stable conditions: 1) *Thermal stability*. Fluctuations of measured temperatures in the fin body should not exceed a pre-determined value of the sensors' uncertainties; 2) *Hydrodynamic stability*. Observed fluctuations of the film thickness on the fin should be within 5%; 3) *Symmetry*. Film profile should be symmetric.
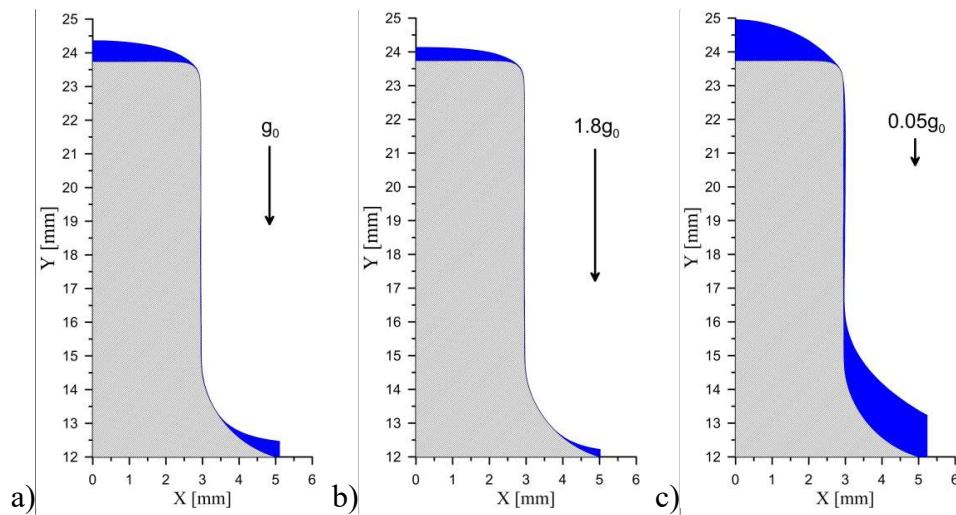

Figure 9. Condensate film (blue) on the fin (grey) at different gravity levels.
$P_v=635$ hPa; $T_{sat}=47.5$ ^oC; $T_{Ph}=35$ ^oC; $g_0=9.8$ m/s^2.

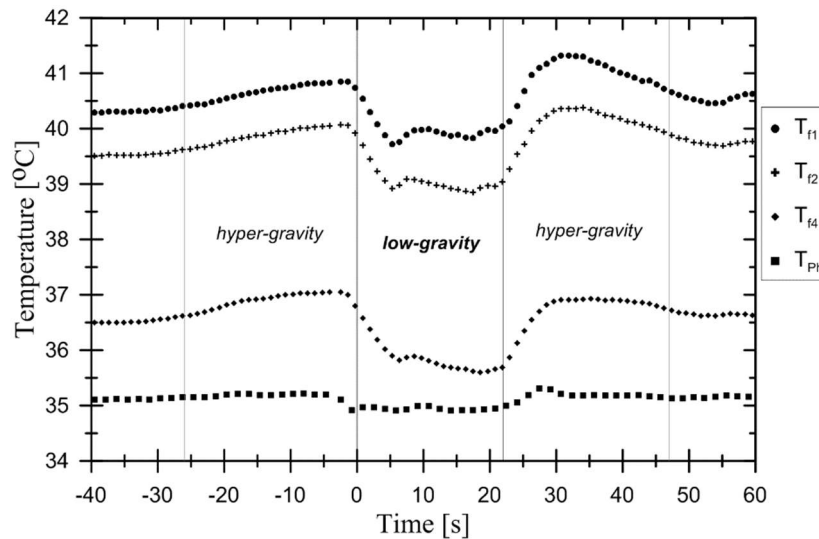**Figure 10.** Evolution of temperatures measured inside fin-sample during one parabola;
$P_v=635$ hPa; $T_{sat}=47.5$ ^oC; $T_{Ph}=35$ ^oC.

13

Figure 11 shows distribution of the total curvature of the film surface along the fin profile under various gravity levels obtained during one parabola. Vertical dashed lines highlight the center of the fin corner. Empty circles correspond to the normal gravity. Squares show data for hyper-gravity taken 10 sec before low gravity period (Figure 10, -10 s). Stable condition reached at the end of the low gravity period (Figure 10, 15-22 s) is shown by the filled triangles. The curvature of the drop at the fin tip increases from a minimum value at the symmetry axis up to a maximum at the fin corner at hyper- and normal gravities (Figure 11). At low-gravity, the drop has a spherical shape (Figure 11, 0-2.5 mm) and its curvature increases only close to the corner. The curvature decreases from its maximum value to the constant level from the corner to the beginning of the lateral wall in all three cases (Figure 11, *2.9-4 mm*). It is interesting that the maximum values of the film curvature are smaller than one of the fin corner (2450 m^{-1}). There are no significant changes of the film profile on the cylindrical part of the fin. Curvature changes two times at the fin bottom at normal and hyper-gravities. The first decrease happens in the arc region 11-12 mm. The liquid levels were lower than this part of the fin (Figure 9) and the thin film surface followed the fin shape in both cases. Therefore we can assume that this film curvature's decrease is induced by the change of the fin geometry from the cylindrical shape to the curved bottom (**Error! Reference source not found.**, 11-12 mm). Second change of the film curvature is located at the arc lengths longer than 13 mm (Figure 11). The thin film joined the liquid meniscus at these locations. Highest condensate levels were observed at low gravity. Therefore the curvature reduction observed in the region 10-11 mm is caused by the transition of the film to the meniscus.
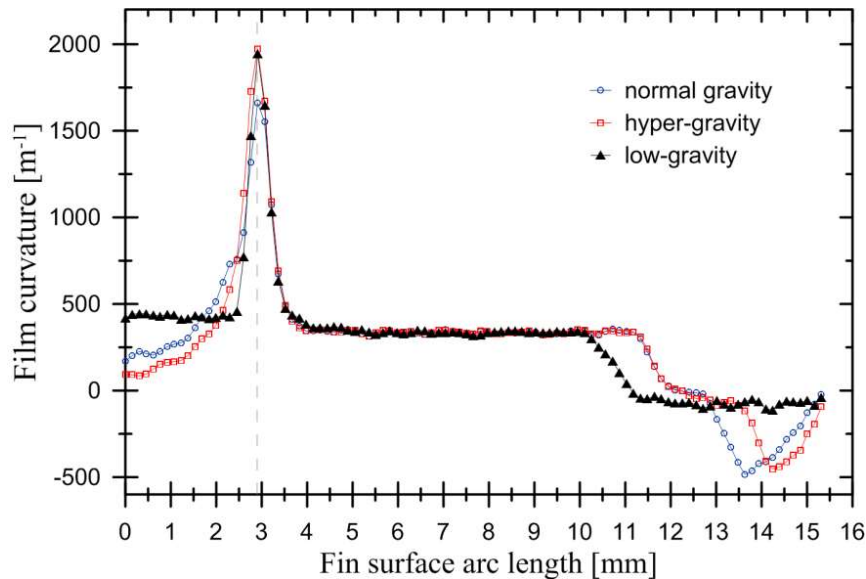

Figure 11. Total curvature of the film surface under various gravity conditions;
Dashed line shows location of the fin corner center;
Conditions: P_v=635 hPa; T_{sat}=47.5 °C; T_{Ph}=35 °C.

Any changes of the condensate surface curvature leads to the appearance of a surface-tension pressure gradient which affects the liquid motion in addition to gravity. Generally, the Bond number is used to describe the ratio between gravitational and capillary forces. In this work the inversed Bond number is introduced using formula (9) in order to reveal areas on the fin where the surface-tension pressure gradient (STPG) has strong influence on the condensate flow.

$$iBo=-(dP_l/ds)/(\rho g)=-(\sigma \cdot d\kappa_{tot}/ds)/(\rho g)\ (9)$$

Figure 12 shows the distribution of the film thickness and the corresponding *iBo* number for different gravity levels. The grey bar in the figure marks the area where the gravitational force has an important influence on the condensate flow (*iBo<1*). The height of the drops is 650 μm, 390 μm and 800 μm for normal, hyper and low gravities, respectively. A very thin film is detected at the fin corner in all cases. It can be explained by a strong STPG (*iBo>>1*). At normal and hyper gravities, the film increases along the lateral surface of the fin (Figure 12 a and b, 4-11 mm). Local thinning of the film can be observed in the areas in which the inversed Bond number is higher than

14

unity: in normal gravity (Figure 12a), this is at 11.7 mm and 13.1 mm and in hyper gravity (Figure 12b) at 11.7 mm and 14 mm. Under low gravity, the film increases first (Figure 12c, 2.9-6.5 mm) and then decreases until the liquid meniscus at the fin bottom (Figure 12c, 11.5-16 mm). The gravitational force is not strong enough to push forward the liquid driven from the fin corner by STPG. A second local minimum of the film thickness is located at 10.5 mm.
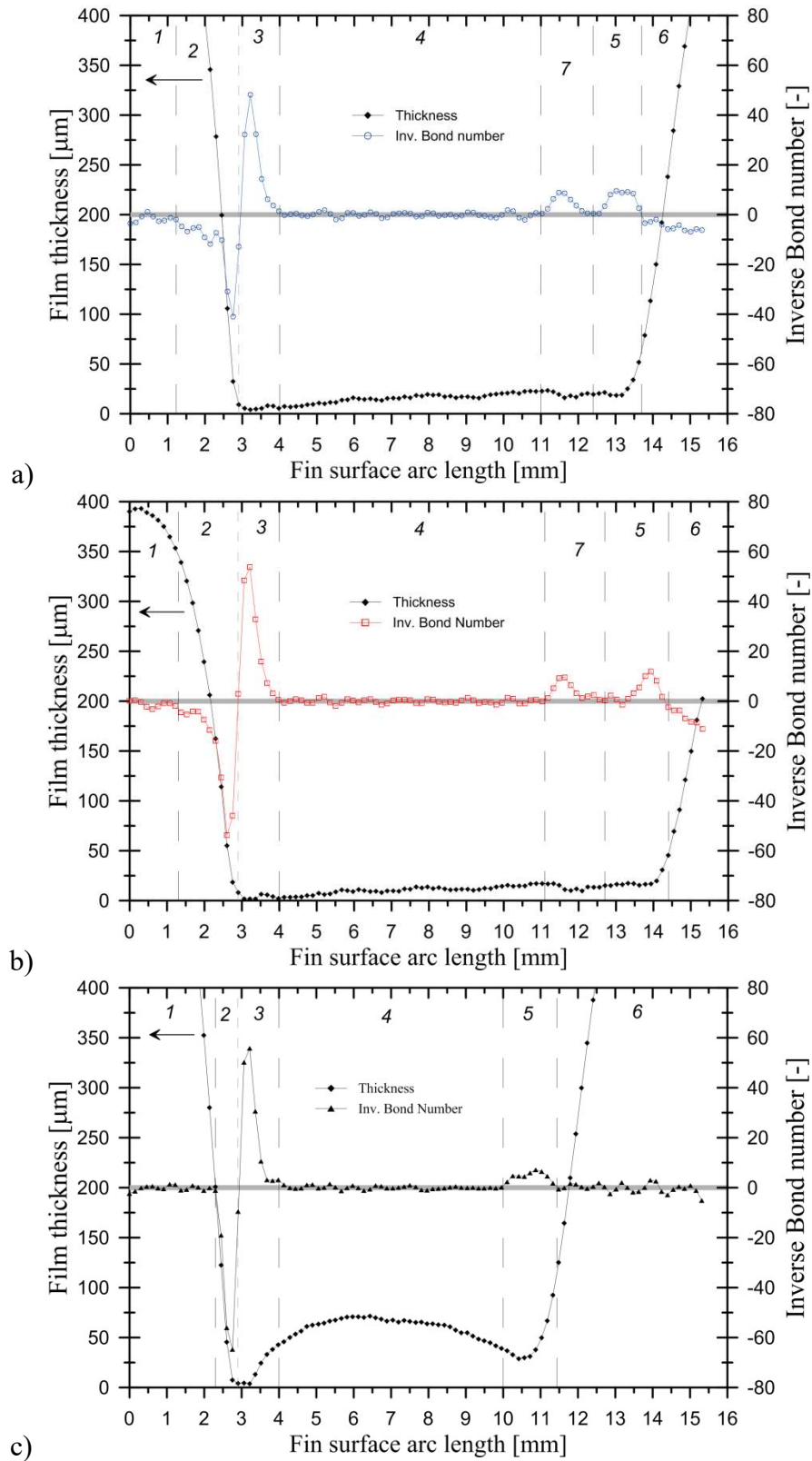

a)

b)

c)

Figure 12. Film thickness distribution and corresponding inversed Bond number along the fin surface: *a) normal gravity; b) hyper-gravity; c) low gravity.*

Analysis of the force balance and thickness distribution of the film reveals that seven areas can be marked out on the fin surface. Each area is labeled by a number in Figure 12 and shown schematically in the Figure 13:

1. First area is the fin tip where the drop exists. Both forces contribute to the drop shape;
2. Second area is the left side of the fin corner. STPG is the main acting force in this region. The negative sign of *iBo* means that the condensate flows from the corner to the fin tip providing the continuous growth of the drop. The length of this region strongly depends on the drop shape.
3. On the other side of the corner, a third region is located. The gradient of surface-tension pressure pushes the condensate in the direction of the fin bottom. It is interesting to note that the dimension of this region does not depend on the gravity level and is equal to the length of the fin curvature change, i.e. 1.1 mm for the fin tested.
4. Fourth region is the cylindrical part of the fin. The gravitational force drives the flow of condensate in this region. Effect of STPG is very small.
5. Fifth area is located at the place where the thin film joins the liquid meniscus. When the transition of the film curvature to the meniscus occurs, one creates STPG which overcomes the gravity. So, in low-gravity this region is located at 10-11.5 mm, at normal gravity it is located at 12.6-13.7 mm and at hyper gravity even at 13.2-14.4 mm.
6. The sixth region is occupied by the fluid meniscus.
7. Seventh area can be seen in case of hyper and normal gravities. It is located between 11 - 12 mm of the fin surface arc length. The curvature of the fin changes in this region. The condensate film follows the fin profile and, as a result, has the same changes as the surface curvature. Seventh region was not detected in the case of low gravity because of important height of liquid level at the fin base.

Obtained data show that the influence of the gradient of surface-tension pressure is very important in two cases. First, any variation of the fin curvature leads to the appearance of STPG. It is observed in the areas 2, 3 and 7. Secondly, STPG affects significantly in the region where the film thickness changes dramatically. For example, the film increases ten times in the fifth region; from a thin film flowing along the lateral wall (area 4) to a huge liquid level at the fin bottom (area 6). STPG did not show any important influence at the cylindrical part of the fin (area 4) even at low gravity level. It is important to notice that the quantity of areas does not depend on gravity level. This confirms the correctness of the fin surface segmentation, as used by various authors [8-10], to simplify the condensation modelling.
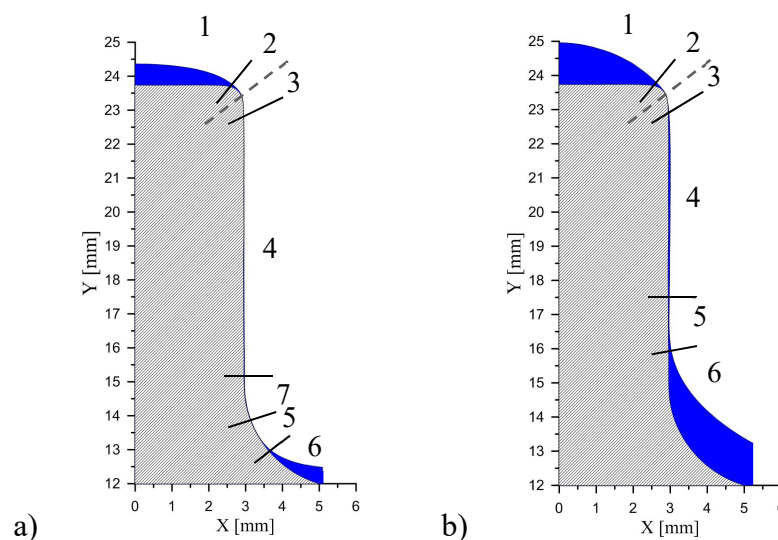

Figure 13. Schematic representation of regions found:
a) normal or hyper gravity; b) low gravity.

The fin used in the experiments was made out of brass (the thermal conductivity of brass is about 100-120 W/(mK)). Figure 14 shows the fin surface temperature at normal and low gravity levels. The temperature distribution under hyper gravity is very close to the one of normal gravity. Therefore it is not presented here. The model of temperature evaluation is described in paragraph 4.2. The temperature of the fin is higher during normal gravity period. The fin tip has uniform temperature in both cases (Figure 14, 0-2 mm). The presence of a big drop at the tip prevents any valuable heat transfer because it has a very high thermal resistance. The hottest area is located at the fin corner as a result of a higher heat flux. The surface temperature decreases from the fin corner to its bottom.
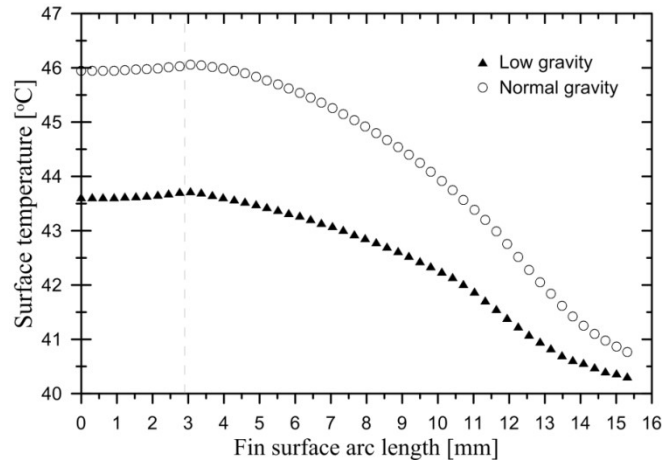

Figure 14. Fin surface temperature at normal and low gravity levels;
Conditions: $P_v=635$ hPa; $T_{sat}=47.5\ ^oC$; $T_{Ph}=35\ ^oC$.

Different behavior of the condensed liquid (thickness, acting forces) in the regions can leads to contrasting heat transfer on the fin surface. Figure 15 shows a heat flux distribution along the fin surface under normal and low gravity conditions. Vertical lines in the figure separates revealed areas. The distribution under hyper gravity is similar to the one of normal gravity, therefore it is not present here. The heat flux is calculated as:

$$q(s)=\lambda_l(T_v-T_{surf}(s))/\delta_{film}(s) \qquad (10)$$

Here s is the fin surface arc length, λ_l is the thermal conductivity of the condensate, δ_{film} is the film thickness, T_v is the vapour temperature and T_{surf} is the fin surface temperature. The heat flux is very small in the regions 1 and 6, because of a high amount of liquid inside. Rapid increase of the heat flux appears in the second area. The heat flux on the cylindrical part of the fin (area 4) at normal gravity is higher than at reduced gravity. Local maximums are detected in areas 3, 5 and 7 where the surface-tension pressure gradient has the greatest influence.
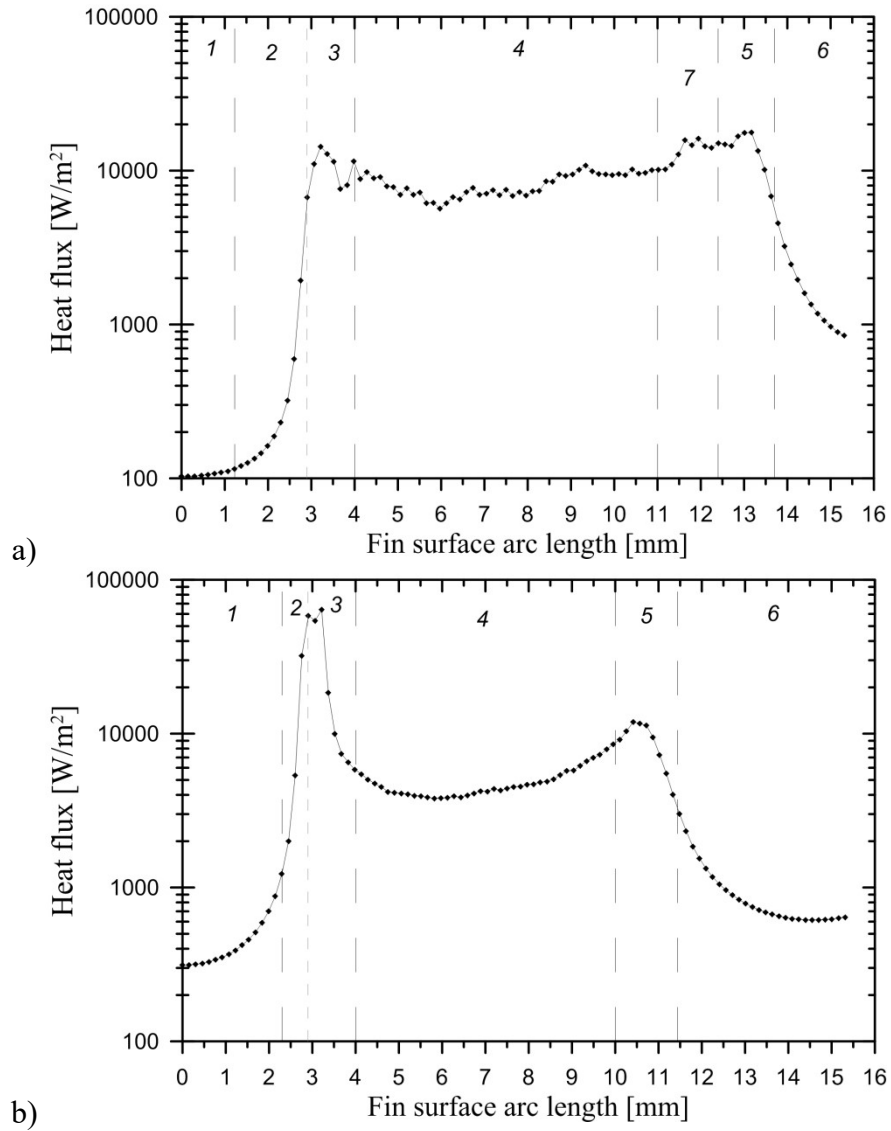
Figure 15. Heat flux distribution at normal (a) and low (b) gravities.

Analysis of the heat flux distribution revealed maximal values in the areas where the surface tension pressure gradient affects strongly the condensate motion. However, a high heat flux in a small area can lead to a negligible contribution for the overall heat transfer. In order to demonstrate the relation between each area and the overall heat transfer, the condensation heat released in each area has been calculated:

$$Q(s_i, s_{i+1}) = 2\pi\lambda_l \int_{s_i}^{s_{i+1}} \frac{X(\tau)}{\delta_{film}(\tau)} \left(T_v - T_{surf}(\tau)\right) d\tau \quad (11)$$

Here s_i and s_{i+1} are boundaries of i area. Figure 16 shows the heat load of each region at various $(T_v - \langle T_{surf} \rangle)$, where $< >$ denotes the average value. The heat loads at hyper gravity is similar to normal gravity and are not shown on the figure. The input of regions 1 and 6 is very small in both cases. The most intensive condensation occurs on the cylindrical part at normal gravity (Figure 16a). Areas with influence of STPG provide 10-15 % of the total heat removed from the fin. It means that inputs of these areas are not negligible even under terrestrial condition. In case of low gravity, the most intensive condensation takes place in region 3 and on the lateral wall (region 4) of the fin. The heat loads in these regions are comparable at a temperature drop of less than 10 K. On another note, region 4 provides more condensate at higher temperatures. The fifth region provides 10-15 % of the total heat load.
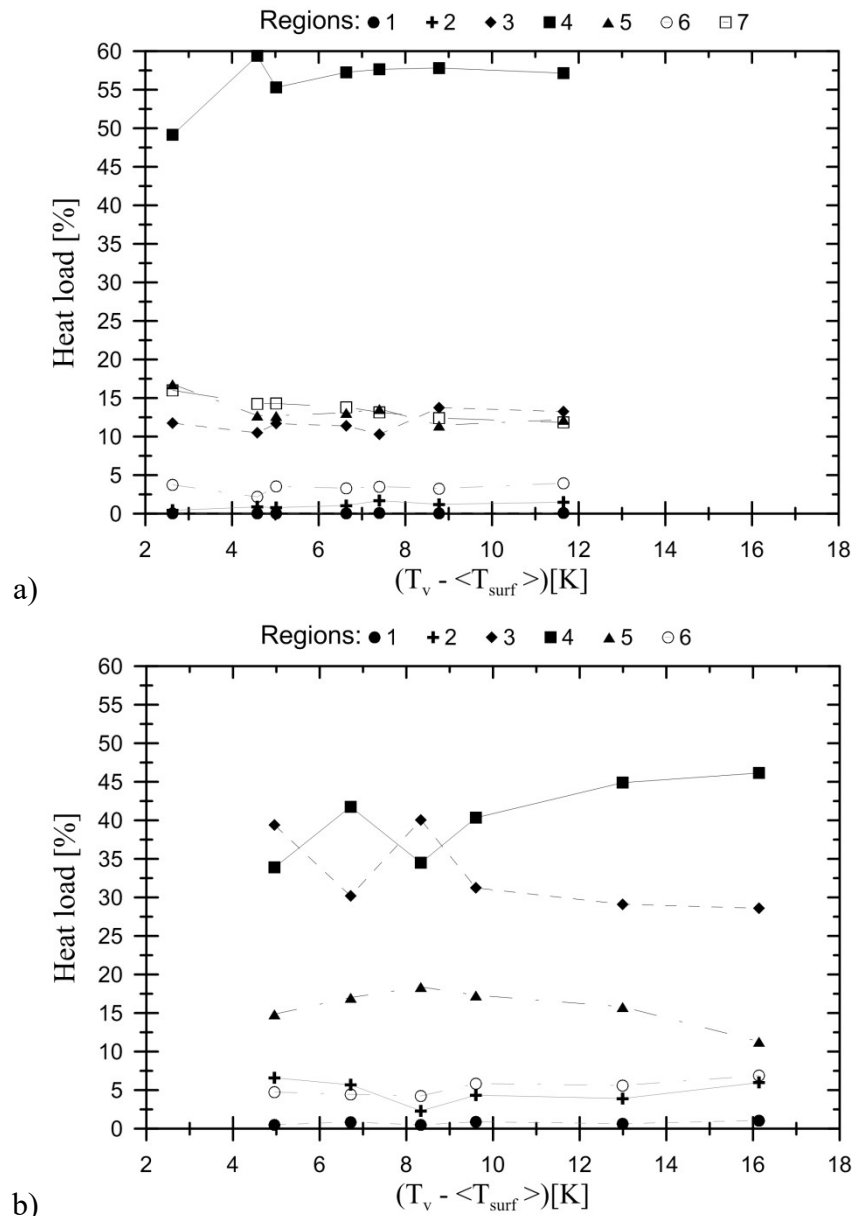
Figure 16. Heat load at fin regions at different temperature drops (T_v-$<T_{surf}>$);
a) normal gravity; b) low gravity.

Heat load analysis shows that areas with high influence of STPG provide significant input to the total heat of condensation. The total input of the areas 3, 5 and 7 is about 39 % at normal gravity. That is comparable with the condensation in the fourth area. Removing one of these regions from consideration leads to non-negligible uncertainty for condensation modelling.

It is interesting to note that the fin corner starts playing an important role under low gravity condition. On the contrary, the gravitational force does not provide a stable condensate flow along the cylindrical surface. By summarizing these results, it is possible to conjecture that rectangular or trapezoidal fins are not suitable for microgravity conditions.

6. Conclusions

Experimental investigation of vapour condensation on a single cylindrical fin has been carried out under various gravity conditions. The experiment has been flown onboard the Airbus A300 Zero-G aircraft by the European Space Agency performing parabolic trajectories during which the gravity has been varied from $1g_0$ (normal gravity) to $1.8g_0$ (hyper gravity) and eventually to $0.05g_0$ (low gravity). A cylindrical fin shape was selected because the obtained data can be interpolated to the rectangular and trapezoidal integral-fin. Considerable attention was given to

19

achieve a stable condensation at low gravity period. Information about the condensate distribution and the fin surface temperature has been obtained.

For the first time, the balance of forces acting on the condensate flow is analyzed. The inversed Bond number is used to describe the ratio between the gravitational force and the surface-tension pressure gradient. STPG is derived from the film surface curvature distribution measured by the afocal optical system. Experimental data show that the influence of STPG is very important in two cases. First, any variation of the fin curvature leads to appearance of STPG. Second, STPG has an important effect in the regions where the film thickness changes several orders of magnitude. Seven areas have been determined on the fin surface depending on the main force acting on the liquid motion. Gravitational force is important at the fin tip, on the lateral fin wall and at the fin base occupied by the liquid. STPG overcomes gravity at both parts of the fin corner, in the area of thin film and meniscus joining. The seventh area affected by STPG appears where the liquid level at the fin base is very low. The magnitude of the areas does not depend on the gravity level. This confirms the correctness of the fin surface segmentation, as used by various authors, to simplify the condensation modelling.

Analysis of the heat flux distribution along the fin surface shows that the areas, where STPG overcomes the gravitational force, have very high values of the heat flux. Fin surface temperature required for heat flux is found from CFD computation of the temperature distribution inside the fin body. Analysis of the heat load shows that each region affected by STPG provides 10-15 % of the total heat load. The contribution of these areas is not negligible and should be taken into account. In case of low gravity, the most intensive condensation takes place at the corner of the fin tip and on its cylindrical part. The heat loads in these regions are comparable. This is the first time that the influences of each force on condensation heat transfer are evaluated from experimental data.

The gravitational force did not provide a stable condensate flow along the cylindrical surface under low gravity condition. Therefore, it is possible to conjecture that rectangular or trapezoidal fins are not suitable for microgravity conditions. This consequently shows the importance of the curvature analysis performed in this work.

References

[1] V. G. Rifert and H. F. Smirnov, Condensation Heat Transfer Enhancement, Southampton, UK: WITpress,2004, pp. 392;

[2] A. Cavallini, G. Censi, D. Del Col, L. Doretti, G.A. Longo, L. Rossetto, C. Zilio, Condensation inside and outside smooth and enhanced tubes – a review of recent research, International Journal of Refrigeration 26 (2003) 373 – 392;

[3] A. Miyara, Condensation of hydrocarbons – A review, International Journal of Refrigeration 31 (4) (2008) 621–632;

[4] J. W. Rose, An approximate equation for the vapour-side heat-transfer coefficient for condensation on low-finned tubes, International Journal of Heat and Mass Transfer 37 (5) (1994) 865-875;

[5] M. A. Kedzierski, J S. Brown, M. Carr, Measurement and Prediction of Vapor-Space Condensation of Refrigerants on Trapezoidal-Finned and Turbo-C Geometries, Journal of Enhanced Heat Transfer 20 (1) (2013) 59-71;

[6] H. Honda, S. Nozu, A Prediction Method for Heat Transfer During Film Condensation on Horizontal Low Integral-Fin Tubes, Journal of Heat Transfer 109 (1987) 218-225;

[7] T. Gebauer, A. R. Al-Badri, A. Gotterbarm, J. El Hajal, A. Leipertz, A. P. Fröba, Condensation heat transfer on single horizontal smooth and finned tubes and tube bundles for R134a and propane, International Journal of Heat and Mass Transfer 56 (1–2) (2013) 516–524;

[8] T. Adamek and R. L. Webb, Prediction of film condensation on horizontal integral fin tubes, International Journal of Heat and Mass Transfer 33 (8) (1990) 1721-1735;

[9] M. Belghazi, A. Bontemps, C Marvillet, Condensation heat transfer on enhanced surface tubes: experimental results and predictive theory, Journal of Heat Transfer 124 (4) (2002) 754-761;

[10] A. R. Al-Badri, T. Gebauer, A. Leipertz, A. P. Fröba, Element by element prediction model of condensation heat transfer on a horizontal integral finned tube, International Journal of Heat and Mass Transfer 62 (2013) 463–472;

[11] E.E. Wilson, A basis of rational design of heat transfer apparatus, Journal of Heat Transfer 37 (1915) 47-70;

[12] J. W. Rose, Heat-transfer coefficients, Wilson plots and accuracy of thermal measurement, Experimental Thermal and Fluid Science 28 (2004) 77-86;

[13] F. J. Uhía, A. Campo, J. Fernández-Seara, Uncertainty analysis for experimental heat transfer data obtained by the Wilson plot method: application to condensation on horizontal plain tubes, Thermal Science 17 (2) (2013) 471-487;

[14] J. Fernández-Seara, F. J. Uhía, R. Dizm Experimental analysis of ammonia condensation on smooth and integral-fin titanium tubes, International Journal of Refrigeration 32 (2009) 1140-1148;

[15] W.-T. Ji, Ch.-Y. Zhao, D.-C. Zhang, Z.Y. Li, Y.-L. He, W.-Q. Tao, Condensation of R134a outside single horizontal titanium, cupronickel (B10 and B30), stainless steel and cupper tubes, International Journal of Heat and Mass Transfer 77 (2014) 194-201;

[16] S. Hirasawa, K. Hijikata, Y. Mori and W. Nakayama, Effect of Surface Tension on Condensate Motion in Laminar Film Condensation (Study of Liquid Film in a Small Trench), International Journal of Heat Mass Transfer 23 (1980) 1471-1478;

[17] M. A. Kedzierski and R. L. Webb, Experimental Measurement of Condensation on Vertical Plates with Enhanced Fins, ASME-Boiling and Condensation in Heat Transfer Equipment 85 (1987) 97-95;

[18] A. Glushchuk, Ch. Minetti and C. Buffone, Fin condensation in variable gravity environment, Multiphase Science and Technology 26 (1) (2014) 63–81;

[19] V. Pletser, Are aircraft parabolic flights really parabolic?, Acta Astronautica, Vol 89, pp. 226–228, 2013;

[20] C. Buffone, V. Grishaev, A. Glushchuk, Experimental investigation of liquid retention in a cyclone evaporator under variable gravity conditions, Applied Thermal Engineering 99 (2016) 235–243;

[21] A.V. Gusarov, I. Smurov, Gas-dynamic boundary conditions of evaporation and condensation: Numerical analysis of the Knudsen layer, Physics of Fluids, 14(12) (2002) 4242-4255.

[22] R.W. Schrage, A Theoretical Study of Interface Mass Transfer, Columbia University Press, New York, 1953, pp. 103;

[23] https://www.scribd.com/doc/49607345/TDS-HFE-7100-Heat-Transfer, accessed on 04 October 2016 at 14:41.